Non-adiabatic imprints on the electron wave packet in strong field ionization with circular polarization

2016 New J. Phys. 18 043011

(http://iopscience.iop.org/1367-2630/18/4/043011)

New Journal of Physics
The open access journal at the forefront of physics

Deutsche Physikalische Gesellschaft DPG
IOP Institute of Physics

Published in partnership with: Deutsche Physikalische Gesellschaft and the Institute of Physics

OPEN ACCESS

RECEIVED
30 October 2015

REVISED
8 March 2016

ACCEPTED FOR PUBLICATION
9 March 2016

PUBLISHED
7 April 2016

PAPER

Non-adiabatic imprints on the electron wave packet in strong field ionization with circular polarization

C Hofmann[1], T Zimmermann[2,3], A Zielinski[4] and A S Landsman[2,3]

[1] Physics Department, ETH Zurich, 8093 Zurich, Switzerland
[2] Seminar for Applied Mathematics, ETH Zurich, 8093 Zurich, Switzerland
[3] Max Planck Institute for the Physics of Complex Systems, Nöthnitzer Straße 38, D-01187 Dresden, Germany
[4] Ludwig Maximilians Universität, Theresienstrasse 37, D-80333 Munich, Germany

E-mail: chofmann@phys.ethz.ch

Keywords: strong field ionization, time-dependent Schrödinger equation, photoelectron momentum distribution, non-adiabatic effects

Abstract

The validity of the adiabatic approximation in strong field ionization under typical experimental conditions has recently become a topic of great interest. Experimental results have been inconclusive, in part, due to the uncertainty in experimental calibration of intensity. Here we turn to the time-dependent Schrödinger equation, where all the laser parameters are known exactly. We find that the centre of the electron momentum distribution (typically used for calibration of elliptically and circularly polarized light) is sensitive to non-adiabatic effects, leading to intensity shifts in experimental data that can significantly affect the interpretation of results. On the other hand, the transverse momentum spread in the plane of polarization is relatively insensitive to such effects, even in the Keldysh parameter regime approaching $\gamma \approx 3$. This suggests the transverse momentum spread in the plane of polarization as a good alternative to the usual calibration method, particularly for experimental investigation of non-adiabatic effects using circularly polarized light.

1. Introduction

This past decade has brought great advances in our ability to capture electron dynamics in ionization of atoms and molecules on the attosecond time-scale (where an attosecond $= 10^{-18}$ s) [1–6]. Our theoretical understanding of this ionization process, the shape of the photoelectron wave packet, and its subsequent propagation form the basis of many measurement techniques in atomic, molecular and optical physics [7, 8]. The interpretation of many experiments in attosecond science is based on the key concept of strong field tunnel ionization. Strong field ionization (SFI) describes an ionization process dominated by very intense laser fields (comparable to the binding potential of the atom), such that the atomic potential is significantly distorted and perturbative calculations are no longer valid. The bending of the Coulomb potential by the time-dependent field leads to tunnel ionization, whereby an electron tunnels out of the atom, predominantly at the peak of the laser field [9–12].

The tunnelling process is frequently modeled using the so-called ADK probability distribution [13–15], which assumes that tunnelling is an adiabatic process, such that the electron tunnels through a static potential barrier (without absorbing quanta of energy from the oscillating electric field). The validity of this adiabatic approximation is determined by the well-known Keldysh parameter [13]

$$\gamma := \frac{\sqrt{2I_p}}{F_{max}}\omega, \tag{1}$$

where I_p is the ionization potential, while ω and F_{max} are the central frequency and the peak field strength of the laser, respectively. The adiabatic limit corresponds to $\gamma \ll 1$. On the other hand, most state-of-the-art experiments operate in the intermediate $\gamma \sim 1$ regime (see for example [16–22]), where the validity of the adiabatic approximation becomes questionable.

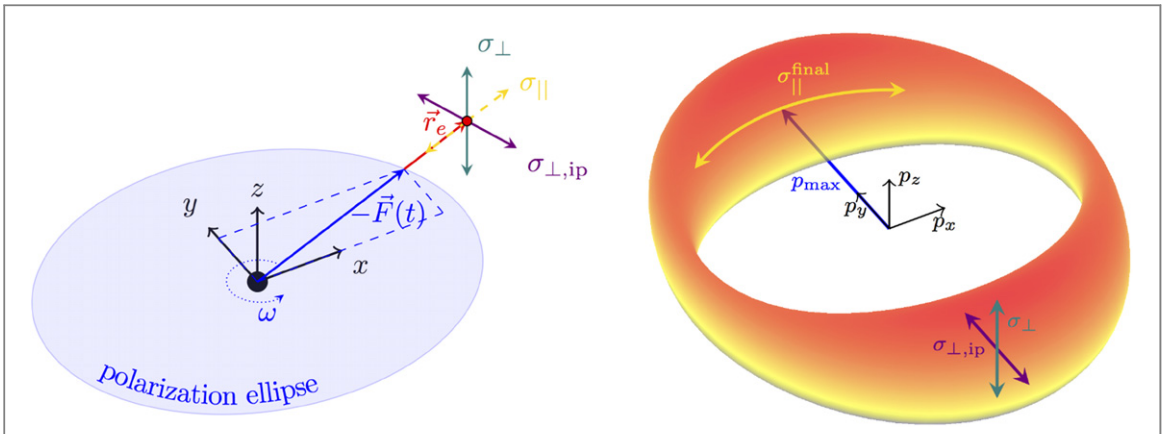

Figure 1. Definition of the coordinate system and momentum spreads. Left: initial conditions for an electron at the exit point $\vec{r}_e$. Right: final momentum distribution for the case of (highly) elliptical polarization. $\sigma_\perp$ is the transverse momentum spread along the laser beam propagation direction z, $\sigma_{\perp,\mathrm{ip}}$ the transverse momentum spread within the plane of polarization, and $\sigma_{||}$ the longitudinal momentum spread.

Therefore, there has been considerable recent interest in the significance of non-adiabatic effects in strong field ionization, with some experiments finding them insignificant in typical experimental regimes [23, 24], while others arriving at the opposite conclusion [25]. A serious source of uncertainty in all these experiments is the calibration of intensity, which is normally achieved using a theoretical model [26, 27]. In particular, the *in situ* field strength has to be reconstructed *a posteriori* from the same experimental data that one wants to study. This leads to a dependence of field strength parameters on the applied theoretical framework. For circular polarization, the intensity is normally calibrated from the radius of the doughnut-shaped electron momentum distribution (see figures 1 and 2) [28]. This calibration procedure usually uses an adiabatic prediction, which corresponds to zero velocity at the tunnel exit for the most probable electron trajectory. However, as we show, this experimental observable is highly sensitive to non-adiabatic effects, as one approaches the $\gamma \approx 2$ regime.

In this work, we solve the time-dependent Schrödinger equation (TDSE) for SFI with circularly polarized light of the simplest rare gas helium in the regime characterized by intermediate values of γ. Since all the laser parameters are known exactly, the TDSE serves as a convenient benchmark to asses the accuracy of both adiabatic and non-adiabatic predictions. We use the radius of the electron momentum distribution extracted from the TDSE solution to establish an optimal calibration procedure, which we then use to re-evaluate the experimental data in [24]. We find non-adiabatic signatures in the transverse momentum distribution of ionized electrons perpendicular to the plane of polarization, indicated by their dependence on the central wavelength of the laser pulse. We also theoretically investigate the sensitivity of various experimental observables to non-adiabatic effects, finding that the transverse momentum spread in the plane of laser polarization is considerably less sensitive to non-adiabatic effects (measured as a function of γ) than the radius of the electron momentum distribution, normally used for calibration. This suggests an alternative experimental calibration procedure for the study of non-adiabatic effects in strong field ionization.

Figure 1 shows the different momentum directions. We define the xy plane to be the plane of polarization. The laser beam propagates in z-direction (see also (5)). It is important to note that the transverse spreads, $\sigma_\perp$ perpendicular to the polarization ellipse (and therefore parallel to the laser beam propagation in z-direction), and $\sigma_{\perp,\mathrm{ip}}$ in the plane of polarization, are conserved from the initial conditions to the final distribution, if the influence of the Coulomb force is neglected. The x and y components of $\sigma_{\perp,\mathrm{ip}}$ at ionization time t are given by

$$\sigma_{\perp,x} = -\sigma_{\perp,\mathrm{ip}} \cdot \sin\left(\arctan\left(\frac{F_y(t)}{F_x(t)}\right)\right), \tag{2}$$

$$\sigma_{\perp,y} = \sigma_{\perp,\mathrm{ip}} \cdot \cos\left(\arctan\left(\frac{F_y(t)}{F_x(t)}\right)\right). \tag{3}$$

The final longitudinal spread $\sigma_{||}^{\mathrm{final}}$ however depends both on the initial spread $\sigma_{||}$ and the ionization phase within the laser cycle. The minor axis radius of the final electron momentum distribution, p_{max}, is the most probable asymptotic drift momentum.

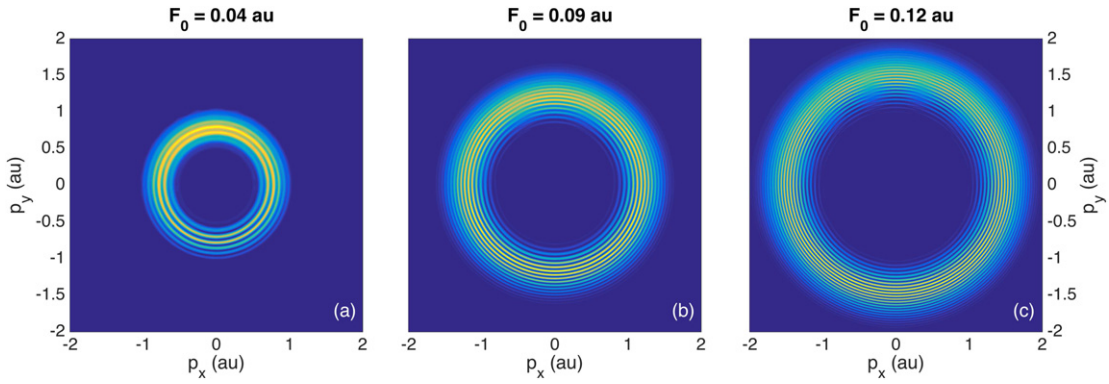

Figure 2. 2D momentum distributions in the polarization plane calculated by TDSE for helium ionized at different electric field strengths.

2. Simulations

2.1. TDSE method

The TDSE describing SFI of helium was solved in velocity gauge using the time-dependent recursive indeXing (tRecX) code [29]. The core idea of this approach is to efficiently solve the TDSE inside a finite size box with finite element discretization, absorbing boundaries to prevent reflection at the edges of the box and to analytically continue the outgoing wave packet outside the box using known Volkov solutions [30].

The single-active electron approximation was employed, which proved to be very accurate for similar problems (see e.g., [26, 31]). Helium was described by the pseudopotential

$$V(r) = \frac{-1 - \exp(-\alpha r)}{r}, \tag{4}$$

where $\alpha = 2.1325$ is chosen such that the ionization energy of the ground state is exactly reproduced. Ionization energies of excited states are also well described by this potential. The 2s excited state energy of the pseudopotential is <0.3 eV from the 1s2s state single ionization potential of helium. The energies of all other single excited states are reproduced by the pseudopotential with errors <0.1 eV. The wave function was expanded in the basis of Legendre polynomial finite elements of order 11 for the radial coordinate and spherical harmonics with the degree $l \leqslant 72$ for the angular (arriving to a total of 88 coefficients) inside the sphere with radius $R = 40$ au. (Unless specified otherwise, atomic units are used throughout this paper.)

Photoelectron spectra were computed using the time-dependent surface flux method (tSURFF) method [30] from the electron flux through the boundary of the simulation box. The reflection from the boundary was prevented by the infinite range exterior complex scaling (irECS) method [32] using 16 Laguerre polynomials to describe the wave function outside the simulation box.

The vector potential had the form

$$\boldsymbol{A}(t) = \frac{F_0}{\omega\sqrt{1+\epsilon^2}}(\sin(\omega t)\hat{\boldsymbol{x}} - \epsilon\cos(wt)\hat{\boldsymbol{y}}) \cdot f(t), \tag{5}$$

corresponding to the laser field $\boldsymbol{F}(t) = -\partial_t \boldsymbol{A}(t)$, where $F_0 = \sqrt{I}$ is the electric field strength connected to the observed intensity, ϵ the ellipticity, ω the frequency, x the major and y the minor axis of the polarization ellipse, and $f(t) = \cos(\pi t/T_{\text{total}})^8$ the envelope. The maximal amplitude of the electric field was therefore $F_{\max} = F_0/\sqrt{1+\epsilon^2} = F_0/\sqrt{2}$ for circular polarization. The pulses used in all TDSE simulations had circular polarization $\epsilon = 1$, wavelength $\lambda = 735$ nm and full width at half-maximum equal to 6 fs, corresponding to a total non-zero time $T_{\text{total}} = 32.4$ fs. The field strengths covered the intermediate range of $\gamma \approx 1$ or slightly larger. The momentum spreads and the most probable final momenta are converged below 0.1% with respect to the the box size, the number of spherical harmonics and the number of finite elements in the radial discretization. Figure 2 shows the calculated momentum distributions in the plane of polarization for different field strengths.

2.2. Analytic approaches

The non-adiabatic theory was initially developed by Perelomov, Popov and Terent'ev (PPT) [33, 34], and sparked many further works, such as [35–38]. These theoretical descriptions all use strong field approximation (SFA), neglecting the influence of the Coulomb force after ionization and assuming unperturbed ground state for the bound wave function. They reduce to the well-known ADK rates [14] in the $\gamma \ll 1$ limit. Additionally,

they all assume that the initial momentum in the direction of the laser field at the tunnel exit, $\sigma_{\parallel}$, is zero. On the other hand, the transverse momentum includes both the direction of laser propagation, $\sigma_{\perp}$, and the plane of laser polarization, $\sigma_{\perp,\mathrm{ip}}$ (see figure 1). For non-adiabatic theories these two quantities are different (see (8) and (9) below), while for ADK they are the same (see (11) below).

For PPT, the final laser cycle averaged momentum distribution consists of two 3D Gaussian lobes (for elliptical polarization) centred around [35]

$$\pm p_{\mathrm{max}}^{\mathrm{NA}} = \pm|\epsilon|\frac{F_0 \sinh \tau_0}{\omega\tau_0\sqrt{1+\epsilon^2}}, \tag{6}$$

where τ_0 is the solution to

$$\sinh^2 \tau_0\left[1-\epsilon^2\left(\coth\tau_0-\frac{1}{\tau_0}\right)^2\right]=\gamma^2. \tag{7}$$

The asymptotic non-adiabatic transverse momentum distributions are expanded into Gaussians. Their widths inside the plane of polarization $\sigma_{\perp,\mathrm{ip}}^{\mathrm{NA}}$ and along the propagation direction of the laser beam $\sigma_{\perp}^{\mathrm{NA}}$ are

$$\sigma_{\perp,\mathrm{ip}}^{\mathrm{NA}} := \sqrt{\frac{\omega}{2c_y}}, \tag{8}$$

$$\sigma_{\perp}^{\mathrm{NA}} := \sqrt{\frac{\omega}{2c_z}}, \tag{9}$$

where c_y and c_z depend on the ellipticity ϵ and τ_0. For circular polarization, the two lobes merge into one rotationally symmetric circular distribution [35].

The quantitative tunnelling Formula (QTF) approach in [38] calculates the probability distribution for a final momentum $\boldsymbol{p}$

$$\begin{aligned}\Gamma^{\mathrm{QTF}}(F_{\mathrm{max}},\,\omega,\,\boldsymbol{p}) = 4\pi\;&|2(\boldsymbol{p}+\tilde{\boldsymbol{A}}(t_{\mathrm{s}}))\cdot\tilde{\boldsymbol{F}}(t_{\mathrm{s}})|^{-1}|\langle\boldsymbol{p}+\tilde{\boldsymbol{A}}(t)|\boldsymbol{r}\cdot\tilde{\boldsymbol{F}}(t)|\psi_0\rangle|^2\\ &\times|\exp(\mathrm{i}S(\boldsymbol{p},\,t_{\mathrm{s}}))|^2\end{aligned} \tag{10}$$

analytically, and includes the often neglected prefactor (first line of (10)) explicitly. $\tilde{\boldsymbol{A}}(t)$ is the vector potential corresponding to the linearly polarized field $\tilde{\boldsymbol{F}}(t) = F_{\mathrm{max}}\cos(\omega t)\hat{\boldsymbol{x}}\cdot f(t)$, ψ_0 represents a hydrogen-like orbital of the initial bound wave function, $S(\boldsymbol{p},\,t_{\mathrm{s}})$ is the action integral, and t_{s} its saddle point [9, 36–38]. QTF represents another non-adiabatic description, but does not yield a closed-form analytic expression for the momentum spreads. Thus, probabilities for different final momenta were calculated, and then fitted with a Gaussian function, see section 2.3 and (13). Because (10) is only given for a linearly polarized field, one can only retrieve $\sigma_{\perp}^{\mathrm{NA}}$, but not $\sigma_{\perp,\mathrm{ip}}^{\mathrm{NA}}$.

Going to the $\gamma\to 0$ limit results in the adiabatic ADK description [9, 13–15], where the transverse width of the momentum distribution is given by

$$\sigma_{\perp}^{\mathrm{A}} = \sigma_{\perp,\mathrm{ip}}^{\mathrm{A}} = \sqrt{\frac{\omega}{2\gamma}} = \sqrt{\frac{F_{\mathrm{max}}}{2\sqrt{2I_{\mathrm{p}}}}} \tag{11}$$

(identical for both transverse directions) and the two lobes are centred around

$$\pm p_{\mathrm{max}}^{\mathrm{A}} = \pm|\epsilon|\frac{F_0}{\omega\sqrt{1+\epsilon^2}}. \tag{12}$$

In this quasistatic picture, ADK can predict an initial transverse momentum distribution at the exit of the tunnel, depending on the instantaneous field strength and direction.

It should be noted that within SFA, the predicted momentum distributions exhibit Gaussian shapes for all the previously discussed theoretical approaches at any ellipticity. However, for small ellipticity the shape of the transverse momentum distribution changes notably, due to the Coulomb focusing for electrons passing close to the ion [39]. Since the present work is focusing on circular (or large ellipticity) polarization, Gaussian functions are well suited in describing the studied momentum distributions. However, the predictive power of SFA is more limited for linearly polarized light, where the electron can return to the vicinity of the parent ion.

Non-adiabatic theories, such as PPT and QTF, describe the asymptotic (rather than the initial) transverse momentum distribution. However, since these theories neglect the Coulomb force during propagation, the initial transverse momentum spread at the tunnel exit is equal to the asymptotic transverse momentum spread (which, in turn, approximates the values measured at the detector). This equivalence arises from the conservation of canonical momentum, whereby the final momentum is equal to the momentum at the tunnel exit shifted by the vector potential at the time of ionization, $A(t_0)$. Hence, the entire momentum distribution is shifted at the detector by $A(t_0)$, preserving the transverse momentum spread.

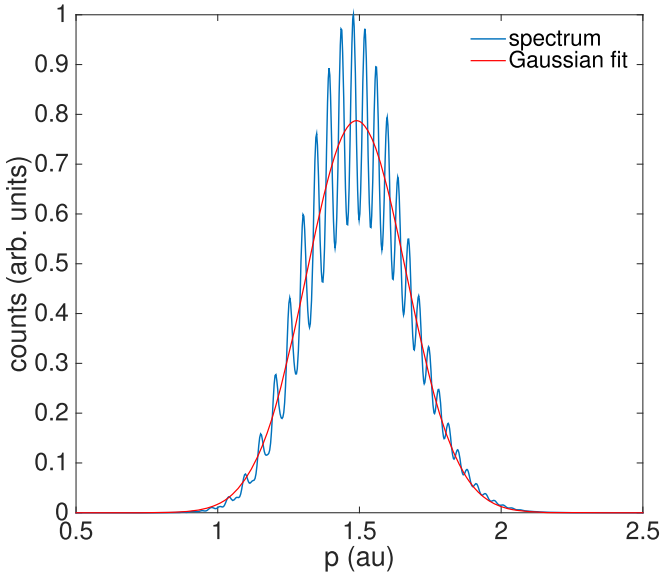

Figure 3. Radial distribution of momenta calculated by TDSE for $F_0 = 0.12$ au (blue curve) overlaid with the Gaussian fit (red curve).

The non-adiabatic theories have frequency depedence in transverse momentum spreads. Their validity is limited by the validity of the saddle point approximation (which breaks down at low intensities). QTF should give a more accurate description of the transverse spread than PPT since it takes a more accurate account of the initial bound wave function through the prefactor. ADK is an adiabatic prediction, which can be derived from PPT in the limit $\gamma \to 0$. The ADK prediction for the transverse spread at the tunnel exit has no frequency dependence and only depends on the instantaneous strength of the laser field. This is because the electron sees a static electric field during the ionization process in the adiabatic limit.

2.3. Comparison with TDSE: transverse momentum spread

To extract the transverse momentum spread in the plane of polarization, $\sigma_{\perp,\mathrm{ip}}$, from the distributions obtained from solution of the TDSE as plotted in figure 2, we integrated over the angle. Figure 3 shows the radial momentum spectrum for the case of $F_0 = 0.12$ au. These spectra were then fitted with a Gaussian function

$$P(p_\perp) = a \exp\left(-\frac{(p_\perp - p_0)^2}{2\sigma_\perp^2}\right), \tag{13}$$

where the amplitude a, the maximum of the distribution p_0 and the width of the distribution $\sigma_\perp$ are free parameters. The fringes visible in both the 2D and radial momentum distributions are due to the interference of wave packets originating from different cycles in the laser pulse. In an experiment where the carrier envelope offset phase is not stabilized, these interferences would average out, resulting in a single Gaussian fit.

Figure 4 shows the extracted transverse momentum spreads $\sigma_{\perp,\mathrm{ip}}$ along with adiabatic ADK (11) and non-adiabatic PPT (8) predictions. The theoretical curves are quite close together, indicating that the transverse momentum spread in the plane of polarization is relatively insensitive to non-adiabatic effects. Because the non-adiabatic and adiabatic predictions are so similar, it is impossible to reliably distinguish between them using TDSE and this particular observable. Agreement with both curves was found to be within 5% or better.

2.4. Comparison with TDSE: final drift momentum

For determining the field strength in SFI experiments, the currently most reliable and accurate method is based on the final drift momentum p_{max} [28, 40], as mentioned above. Neglecting the Coulomb force after ionization (SFA), the final momentum of an individual photoelectron corresponds to the vector potential at the time t_0 when it exits the barrier, plus an initial momentum at the tunnel exit:

$$\boldsymbol{p}^{\mathrm{SFA}} = -\boldsymbol{A}(t_0) + \boldsymbol{p}_0. \tag{14}$$

Figure 5 depicts the extracted p_{max} from the TDSE calculations, compared to adiabatic and non-adiabatic predictions. It is evident that the non-adiabatic theory (6) reproduces the transverse drift momentum much better than the adiabatic ADK description (12), reaching agreement within 3%. On the other hand, the discrepancy between the extracted values and the adiabatic theory is, even for the case of $\gamma \approx 1$, at 8% or worse for lower field strengths. Note, that this is in contrast to the transverse momentum spread $\sigma_{\perp,\mathrm{ip}}$, which seems

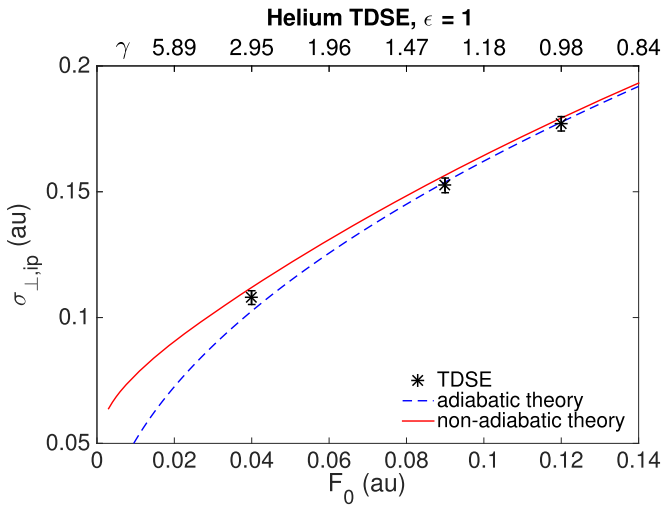

Figure 4. Transverse momentum spread in the plane of polarization extracted from TDSE calculations compared to adiabatic and non-adiabatic theoretical predictions. Error bars represent the 95% confidence interval for the fitting parameters.

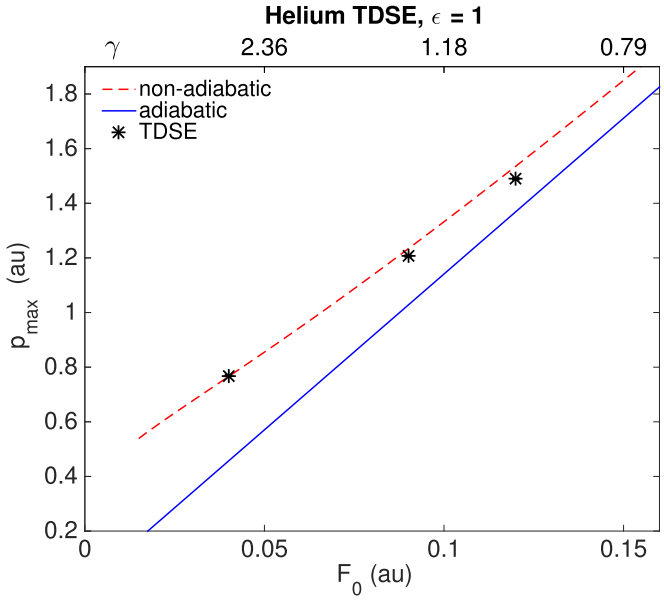

Figure 5. Most probable final momentum as found in TDSE calculations of helium (*) compared to adiabatic (blue solid line) and non-adiabatic (red dashed line) predictions.

much less sensitive to non-adiabatic effects, to the extent that the TDSE cannot reliably distinguish between the adiabatic and non-adiabatic theories (compare figure 4 and section 3).

2.5. Single classical trajectories

In addition to the TDSE solutions of helium, single classical trajectories were calculated. The starting conditions were chosen as the most probable initial conditions at the tunnel exit predicted by the respective theories. This ensures that the single classical trajectory calculation yields the peak in the final momentum distribution $p_{\max}$. For the adiabatic description, the initial momentum at the exit of the tunnel and the exit radius are given by [9, 41]

$$\boldsymbol{p}_0^{\mathrm{A}} = 0, \qquad r_{\mathrm{e}}^{\mathrm{A}} = \frac{I_{\mathrm{p}} + \sqrt{I_{\mathrm{p}}^2 - 4\left(1 - \frac{\sqrt{2I_{\mathrm{p}}}}{2}\right)F_{\max}}}{2F_{\max}} \tag{15}$$

and for the non-adiabatic description [34, 35]

$$|p_{0,\perp,\mathrm{ip}}^{\mathrm{NA}}| = \frac{|\epsilon|F_0}{\omega\sqrt{1+\epsilon^2}}\left(\frac{\sinh\tau_0}{\tau_0} - 1\right),$$
$$r_{\mathrm{e}}^{\mathrm{NA}} = \frac{F_0}{\omega^2\sqrt{1+\epsilon^2}}\cosh\tau_0. \tag{16}$$

The non-adiabatic most probable initial momentum $\boldsymbol{p}_0^{\mathrm{NA}}$ is directed in the $\sigma_{\perp,\mathrm{ip}}$ direction, perpendicular to the electric field at the peak and inside the plane of polarization, in the rotation direction of the field. The classical equations of motion included the Stark shift and induced dipole in the remaining ion

$$\ddot{\boldsymbol{r}}(t) = -\boldsymbol{F}(t) - \boldsymbol{\nabla}\left[\frac{-1}{\sqrt{r^2(t)+\mathrm{SC}}} - \alpha_{\mathrm{I}}\frac{\boldsymbol{F}(t)\cdot\boldsymbol{r}(t)}{r^3(t)}\right], \tag{17}$$

where α_{I} is the polarizability of the ion and $\mathrm{SC} = 0.1\ \mathrm{au}^2$ is the soft core constant to avoid the Coulomb singularity. For small ions, the influence of the induced dipole is negligibly small, such that a comparison to the TDSE calculation with a static pseudopotential is still valid. For larger ions, however, the induced dipole becomes important [42], which is why this type of calculation is used when calibrating experimental data, rather than computationally expensive TDSE calculations. See [26, 41, 42] for more details on the classical trajectory calculations.

For helium, neon and argon, such trajectories were calculated over a large range of field strengths. The resulting $p_{\mathrm{max}}^{\mathrm{A}}(F_0)$ and $p_{\mathrm{max}}^{\mathrm{NA}}(F_0)$ curves for neon and argon were then used for calibration of the experimental data discussed in section 4. The helium curves are plotted in figure 5.

3. Calibration sensitivity to non-adiabatic effects

When investigating non-adiabatic effects in experimental observables, ideally one would want to calibrate the field strength of the data based on a robust observable, and then check a sensitive observable against adiabatic and non-adiabatic theoretical predictions. Figure 5 demonstrates the importance of appropriate field strength calibration in the intermediate or higher γ regime. Had the TDSE electron momentum distributions been calibrated using the adiabatic prediction for the final drift momentum (12), the reconstructed field strengths would have been significantly higher than the actual values used in the simulations. In contrast, calibrating with the transverse momentum spread in the plane of polarization results in a much smaller difference in the reconstructed field strengths between the adiabatic and non-adiabatic predictions, see figure 4.

Equation (16) shows that the offset between the non-adiabatic and adiabatic descriptions for p_{max} grows substantially with increasing ellipticity, explaining the significant difference between the two curves in figure 5 with circular polarization. This observation is further quantified in figure 6, where we plot the relative difference between adiabatic ADK [9, 13–15] and non-adiabatic PPT theory [33–35] for the three observables discussed in this work.

Field strength calibration of experimental data is typically based on analytic adiabatic ADK predictions or classical trajectory calculations within the same framework [24, 28]. Since p_{max} scales approximately with the field strength (see (12)), neglecting non-adiabatic effects and using ADK predictions to calibrate experimental data results in an error of the same order as the error in the p_{max} prediction itself, shown as red dashed line in figure 6. p_{max}, in turn, is sensitive to non-adiabatic effects for close-to-circularly polarized light. This sensitivity is the result of the non-zero transverse velocity (16) at the tunnel exit for the most probable electron trajectory (by contrast, the adiabatic theory predicts this transverse velocity to always be zero (15)). This initial transverse velocity approaches zero in the adiabatic limit, but becomes quite substantial (relative to the radius of the final electron momentum distribution) as γ increases.

The transverse spreads, on the other hand, scale approximately with the square root of the field strength (see (11)). The relative error in the field strength calibration based on this observable introduced by neglecting non-adiabatic effects is therefore approximately twice the error of the spread itself, shown as a green dotted line for the case of $\sigma_{\perp,\mathrm{ip}}$, and blue dotted for $\sigma_{\perp}$ in figure 6. Evidently, $\sigma_{\perp,\mathrm{ip}}$ is the least affected by non-adiabatic effects. For the range of γ studied here, it is always at least a factor of four times smaller than the error in p_{max} based field strength calibration. For example, at $\gamma = 2$, $p_{\mathrm{max}}^{\mathrm{NA}}$ is about 44% larger than $p_{\mathrm{max}}^{\mathrm{A}}$, whereas the error for field strength calibration using the transverse spread $\sigma_{\perp,\mathrm{ip}}$ is only about 10%.

As figure 6 shows, the transverse momentum spread along the direction of laser propagation, $\sigma_{\perp}$, is less sensitive to non-adiabatic effects than the drift momentum, but more sensitive than the transverse spread in the plane of polarization. It follows that the transverse spread in the plane of polarization is the most robust (of the observables investigated) to differences between adiabatic and non-adiabatic predictions. It may therefore be a good alternative to standard calibration methods for experiments further searching for non-adiabatic

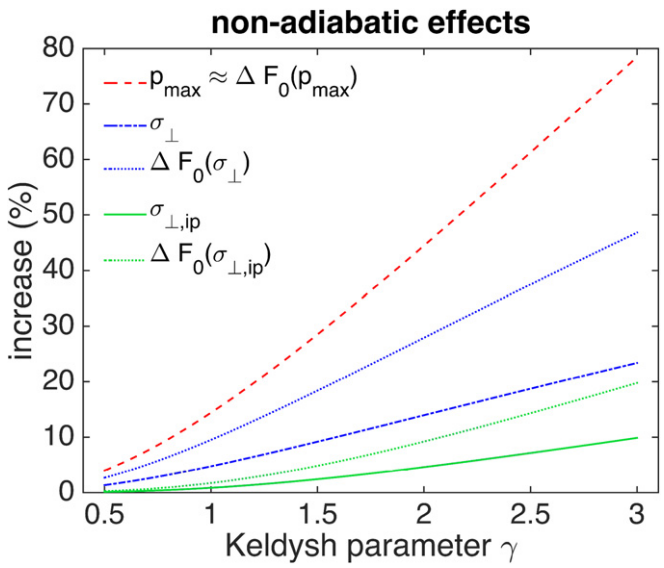

Figure 6. Predicted increase of the observables due to non-adiabatic effects for the final drift momentum p_{max} (red dashed), the transverse momentum along the propagation direction $\sigma_\perp$ (blue dotted–dashed), the transverse momentum spread in plane of polarization $\sigma_{\perp,ip}$ (green solid), as well as the errors for F_0 calibration introduced by neglecting non-adiabatic effects (blue and green dotted) when looking at the transverse momentum spreads.

signatures, or other SFI experiments in the intermediate range of γ. In a recent publication, Li and coworkers came to a similar conclusion [43].

4. Assessment of experimental results

In an experiment by Arissian and coworkers, the authors investigated the photoelectron momentum distribution from argon and neon along the laser propagation direction $\sigma_\perp$ [24], with specific focus on the search for non-adiabatic effects. In the adiabatic description, the width of this momentum distribution only depends on the ionization potential of the target and the amplitude of the ionising field, see (11). On the other hand, the non-adiabatic description also predicts a dependence on the wavelength, see (9).

The measured data, as presented[5] in [24], was calibrated adiabatically, using (12), and is plotted in figures 7(a) for neon and (b) for argon. In the case of argon, the independence of the transverse spread $\sigma_\perp$ on wavelength (800 versus 1400 nm), suggests an absence of non-adiabatic effects for experimental parameters with γ between 0.9 and 1.5, as was concluded in [24]. However, figure 5 and section 3 showed that this method of field strength calibration is highly sensitive to non-adiabatic effects. Recalibrating the same data based on the non-adiabatic description (6) leads to lower field strengths for the same measurements. The recalibrated data is plotted in figures 7(c) and (d), revealing a smaller transverse momentum spread $\sigma_\perp$ for the 1400 nm ionized values than for 800 nm ionization. Moreover, the *difference* in transverse spreads between the two wavelengths was found to be very close to the prediction of the non-adiabatic PPT theory (9), as demonstrated by the two dotted lines in figure 7(d), which are the two PPT curves shifted up by a constant value of 0.02 au.

In [38], the authors compared their non-adiabatic QTF prediction against the same experimental data from [24]. They found an agreement within error bars between QTF (10) and the adiabatically calibrated argon data for the case of 800 nm ionising field, see figure 7(b). We added the same calculation for the case of 1400 nm ionising field, showing that the experimental measurement is higher than the QTF prediction, see again figure 7(b). Overall, using non-adiabatically calibrated data brings greater consistency to the QTF predictions for 800 and 1400 nm (respectively) as well as for both neon and argon, showing that the difference between the theory and experiment is comparable between the two targets and different wavelengths, see figures 7(c) and (d).

To conclude, if non-adiabatic calibration is applied to the experimental measurements of argon in [24] (where two different laser wavelengths were used), then a clear dependence of the transverse momentum spread $\sigma_\perp$ on wavelength is observed, indicating the presence of non-adiabatic effects. However, this wavelength dependence disappears if adiabatic calibration is used, which lead the authors in [24] to conclude the absence of non-adiabatic effects. Moreover, the experimentally observed increase in the transverse spread $\sigma_\perp$ of argon with

[5] The authors of [24] use the non-standard $\exp(-x^2/\sigma^2)$ Gaussian definition, such that the numerical values shown here are given by $\sigma_\perp = \sigma/\sqrt{2}$ (see (13)).

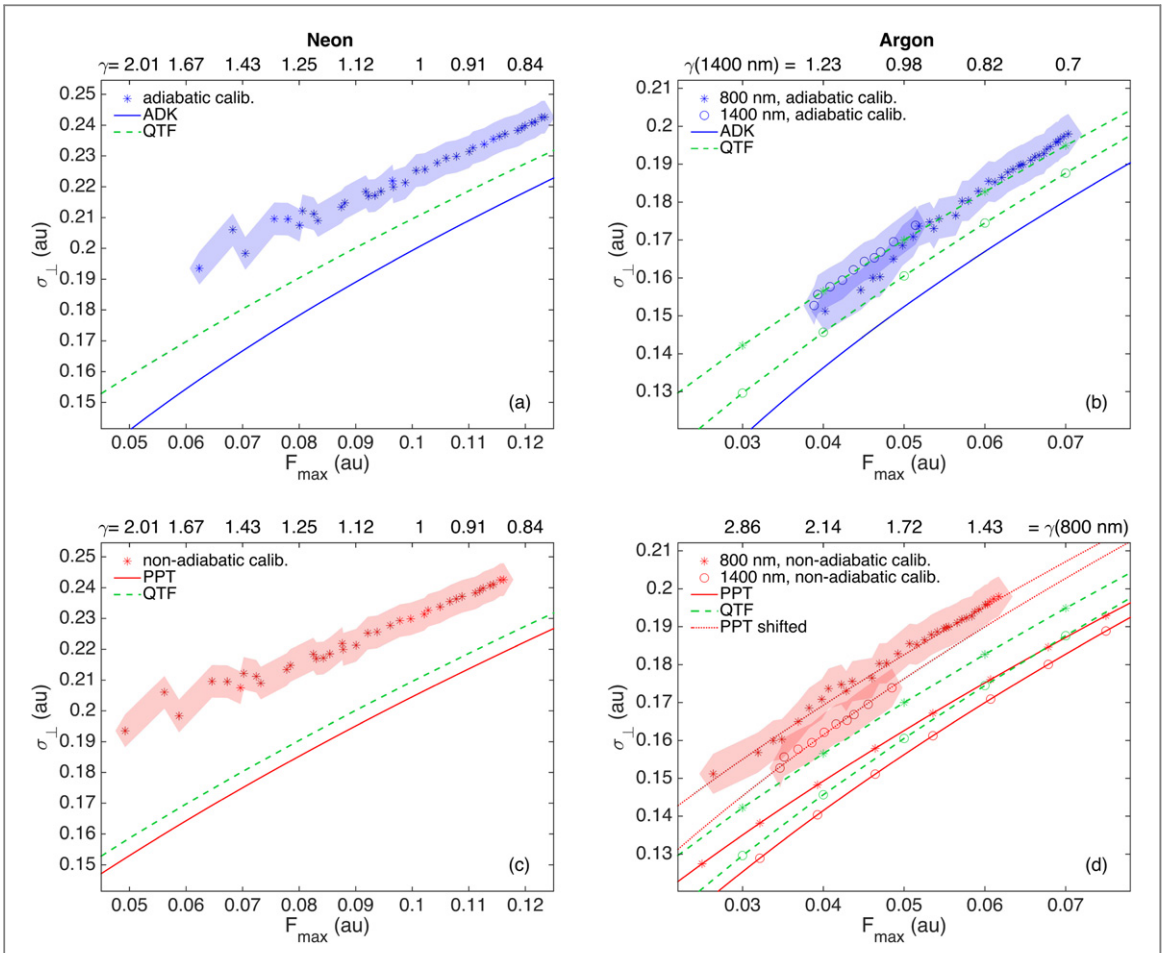

Figure 7. Transverse momentum spreads along beam propagation $\sigma_\perp$ from neon (a)+(c) and argon (b)+(d), where the field strength of the data is adiabatically (a)+(b) or non-adiabatically (c)+(d) calibrated. For all cases, the corresponding predictions of the non-adiabatic QTF (10) is plotted as green dashed curves. Blue solid curves show the adiabatic ADK predictions (11), red solid curves the non-adiabatic PPT (9). To distinguish the two wavelengths for argon, * is used for 800 nm and ○ for 1400 nm. (d): Dotted curves show the PPT predictions shifted up.

increasing frequency (for non-adiabatically calibrated data) is consistent with predictions of the non-adiabatic theories.

Although non-adiabatic theory can accurately predict the increase in transverse spread along beam propagation with increasing frequency, there remains a gap between the total momentum spread predicted by the theory (adiabatic or otherwise) and the experimental measurements. We cannot explain this gap at present. One possible reason was already mentioned in [38] specific for the QTF approach, that the initial bound wave function is not well enough approximated by the hydrogen-like orbitals. Another possible reasons could be multielectron effects, or some unquantified source of experimental uncertainty (since any uncertainty would add to the total variance of the transverse spread).

5. Outlook

TDSE calculations for (small enough) atoms served as ideal experiment for studying the transverse momentum distribution in the plane of polarization in an intermediate Keldysh parameter γ regime. The results showed very good agreement within 5% or better with standard non-adiabatic theory and confirmed the significance of non-adiabatic effects.

Adopting this established non-adiabatic field strength calibration allowed us to resolve some of the issues raised in SFI experiments of recent years. We showed that by making use of non-adiabatic field strength calibration, the predicted wavelength scaling of the transverse momentum spread along beam propagation was beautifully reproduced in the experiment of [24]. Additionally, the previously puzzling difference in explanatory power of the QTF approach [38] was cleared up, by showing that the difference between the QTF prediction and the non-adiabatically calibrated measurements is comparable for both argon and neon data. Still, there remains more theoretical work to be done to explain the remaining quantitative difference.

Lastly, we also showed that the transverse momentum spread observable in the plane of polarization is far more robust against non-adiabatic effects than the drift momentum observable normally used for field strength calibration, suggesting an alternative calibration method in the non-adiabatic regime.

Acknowledgments

This research was supported by the NCCR MUST, funded by the Swiss National Science Foundation (SNSF), an SNSF project grant and an SNSF mobility grant. TZ and ASL acknowledge the Max Planck Centre of Attosecond Science (MPC-AS). AZ acknowledges support by the excellence cluster 'Munich Center for Advanced Photonics (MAP)' and by the Austrian Science Foundation project ViCoM (Grant No. F41).

We acknowledge valuable insights from Ursula Keller and Armin Scrinzi.

References

[1] Kraus P M *et al* 2015 Measurement and laser control of attosecond charge migration in ionized iodoacetylene *Science* **350** 790–5
[2] Schultze M *et al* 2014 Attosecond band-gap dynamics in silicon *Science* **346** 1348–52
[3] Blaga C I, Xu J, DiChiara A D, Sistrunk E, Zhang K, Agostini P, Miller T A, DiMauro L F and Lin C D 2012 Imaging ultrafast molecular dynamics with laser-induced electron diffraction *Nature* **483** 194–7
[4] Wörner H J, Bertrand J B, Kartashov D V, Corkum P B and Villeneuve D M 2010 Following a chemical reaction using high-harmonic interferometry *Nature* **466** 604–7
[5] Schultze M *et al* 2010 Delay in photoemission *Science* **328** 1658–62
[6] Goulielmakis E *et al* 2008 Single-cycle nonlinear optics *Science* **320** 1614–7
[7] Krausz F and Ivanov M 2009 Attosecond physics *Rev. Mod. Phys.* **81** 163–234
[8] Gallmann L, Cirelli C and Keller U 2012 Attosecond science: recent highlights and future trends *Annu. Rev. Phys. Chem.* **63** 447–69
[9] Ivanov M Y, Spanner M and Smirnova O 2005 Anatomy of strong field ionization *J. Mod. Opt.* **52** 165–84
[10] Corkum P B 1993 Plasma perspective on strong field multiphoton ionization *Phys. Rev. Lett.* **71** 1994–7
[11] Faizal F H M 1973 Multiple absorption of laser photons by atoms *J. Phys. B: At. Mol. Phys.* **6** L89–92
[12] Reiss H R 1980 Effect of an intense electromagnetic field on a weakly bound system *Phys. Rev.* A **22** 1786–813
[13] Keldysh L V 1965 Ionization in the field of a strong electromagnetic wave *Sov. Phys. JETP* **20** 1307 (www.jetp.ac.ru/cgi-bin/e/index/e/20/5/p1307?a=list)
[14] Ammosov M V, Delone N B and Krainov V P 1986 Tunnel ionization of complex atoms and atomic ions by an alternating electromagnetic field *Sov. Phys. JETP* **64** 1191–4 (www.jetp.ac.ru/cgi-bin/e/index/e/64/6/p1191?a=list)
[15] Delone N B and Krainov V P 1991 Energy and angular electron spectra for the tunnel ionization of atoms by strong low-frequency radiation *J. Opt. Soc. Am.* B **8** 1207–11
[16] Shafir D, Soifer H, Bruner B D, Dagan M, Mairesse Y, Patchkovskii S, Ivanov M Y, Smirnova O and Dudovich N 2012 Resolving the time when an electron exits a tunnelling barrier *Nature* **485** 343–6
[17] Hickstein D D *et al* 2012 Direct visualization of laser-driven electron multiple scattering and tunneling distance in strong-field ionization *Phys. Rev. Lett.* **109** 073004
[18] Odenweller M *et al* 2014 Electron emission from h2+ in strong laser fields *Phys. Rev.* A **89** 013424
[19] Wolter B, Pullen M G, Baudisch M, Sclafani M, Hemmer M, Senftleben A, Schröter C D, Ullrich J, Moshammer R and Biegert J 2015 Strong-field physics with mid-ir fields *Phys. Rev.* X **5** 21034
[20] Landsman A S, Hofmann C, Pfeiffer A N, Cirelli C and Keller U 2013 Unified approach to probing Coulomb effects in tunnel ionization for any ellipticity of laser light *Phys. Rev. Lett.* **111** 263001
[21] Landsman A S, Pfeiffer A N, Hofmann C, Smolarski M, Cirelli C and Keller U 2013 Rydberg state creation by tunnel ionization *New J. Phys.* **15** 13001
[22] Landsman A S, Weger M, Maurer J, Boge R, Ludwig A, Heuser S, Cirelli C, Gallmann L and Keller U 2014 Ultrafast resolution of tunneling delay time *Optica* **1** 343
[23] Boge R, Cirelli C, Landsman A S, Heuser S, Ludwig A, Maurer J, Weger M, Gallmann L and Keller U 2013 Probing non-adiabatic effects in strong-field tunnel ionization *Phys. Rev. Lett.* **111** 103003
[24] Arissian L, Smeenk C, Turner F, Trallero C, Sokolov A V, Villeneuve D M, Staudte A and Corkum P B 2010 Direct test of laser tunneling with electron momentum imaging *Phys. Rev. Lett.* **105** 133002
[25] Pedatzur O *et al* 2015 Attosecond tunnelling interferometry *Nat. Phys.* **11** 815–9
[26] Hofmann C, Landsman A S, Zielinski A, Cirelli C, Zimmermann T, Scrinzi A and Keller U 2014 Interpreting electron-momentum distributions and nonadiabaticity in strong-field ionization *Phys. Rev.* A **90** 043406
[27] Kielpinski D, Sang R T and Litvinyuk I V 2014 Benchmarking strong-field ionization with atomic hydrogen *J. Phys. B: At. Mol. Opt. Phys.* **47** 204003
[28] Alnaser A S, Tong X M, Osipov T, Voss S, Maharjan C M, Shan B, Chang Z and Cocke C L 2004 Laser-peak-intensity calibration using recoil-ion momentum imaging *Phys. Rev.* A **70** 23413
[29] A. Scrinzi *et al* 2015 tRecX (http://homepages.physik.uni-muenchen.de/ armin.scrinzi/tRecX/)
[30] Tao L and Scrinzi A 2012 Photo-electron momentum spectra from minimal volumes: the time-dependent surface flux method *New J. Phys.* **14** 13021
[31] Lucchini M, Ludwig A, Zimmermann T, Kasmi L, Herrmann J, Scrinzi A, Landsman A S, Gallmann L and Keller U 2015 Anisotropic emission in quantum-beat spectroscopy of helium excited states *Phys. Rev.* A **91** 063406
[32] Scrinzi A 2010 Infinite-range exterior complex scaling as a perfect absorber in time-dependent problems *Phys. Rev.* A **81** 053845
[33] Perelomov A M, Popov V S and Terent'ev M V 1966 Ionization of atoms in an alternating electric field *Sov. Phys. JETP* **23** 924 (www.jetp.ac.ru/cgi-bin/e/index/e/23/5/p924?a=list)
[34] Perelomov A M, Popov V S and Terent'ev M V 1967 Ionization of atoms in an alternating electric field: II *Sov. Phys. JETP* **24** 207–17 (www.jetp.ac.ru/cgi-bin/e/index/e/24/1/p207?a=list)

[35] Mur V, Popruzhenko S and Popov V 2001 Energy and momentum spectra of photoelectrons under conditions of ionization by strong laser radiation (the case of elliptic polarization) *Sov. Phys. JETP* **92** 777–88
[36] Yudin G L and Ivanov M Y 2001 Nonadiabatic tunnel ionization: looking inside a laser cycle *Phys. Rev.* A **64** 13409
[37] Bondar D 2008 Instantaneous multiphoton ionization rate and initial distribution of electron momentum *Phys. Rev.* A **78** 015405
[38] Dreissigacker I and Lein M 2013 Quantitative theory for the lateral momentum distribution after strong-field ionization *Chem. Phys.* **414** 69–72
[39] Rudenko A, Zrost K, Ergler Th, Voitkiv A B, Najjari B, de Jesus V L B, Feuerstein B, Schröter C D, Moshammer R and Ullrich J 2005 Coulomb singularity in the transverse momentum distribution for strong-field single ionization *J. Phys. B: At. Mol. Opt. Phys.* **38** L191–8
[40] Geng J-W, Qin L, Li M, Xiong W-H, Liu Y, Gong Q and Peng L-Y 2014 Nonadiabatic tunneling ionization of atoms in elliptically polarized laser fields *J. Phys. B: At. Mol. Opt. Phys.* **47** 204027
[41] Hofmann C, Landsman A S, Cirelli C, Pfeiffer A N and Keller U 2013 Comparison of different approaches to the longitudinal momentum spread after tunnel ionization *J. Phys. B: At. Mol. Opt. Phys.* **46** 125601
[42] Pfeiffer A N, Cirelli C, Smolarski M, Dimitrovski D, Abu-samha M, Madsen L B and Keller U 2012 Attoclock reveals natural coordinates of the laser-induced tunnelling current flow in atoms *Nat. Phys.* **8** 76–80
[43] Li M, Geng J-W, Han M, Liu M-M, Peng L-Y, Gong Q and Liu Y 2016 Subcycle nonadiabatic strong-field tunneling ionization *Phys. Rev.* A **93** 013402